NONLINEAR ELECTROMAGNETIC-THERMAL MODELING USING TIME DOMAIN FINITE ELEMENT METHOD IN THE MACHINERY DESIGN

BY

HONGLIANG LI

THESIS

Submitted in partial fulfillment of the requirements
for the degree of Master of Science in Electrical and Computer Engineering
in the Graduate College of the
University of Illinois at Urbana-Champaign, 2020

Urbana, Illinois

Adviser:

Professor Jianming Jin

ABSTRACT

In this thesis, an electromagnetic-thermal co-simulation algorithm is developed for the three-dimensional modeling of electric machines. To couple electromagnetic (EM) and heat transfer processes, the time-domain finite element method is employed for its capability of modeling complex geometries. Losses generated from EM fields lead to temperature increase, while the temperature change, in turn, modifies material properties and thus affects EM field distribution. An efficient and accurate EM-thermal scheme is proposed to fully couple these two phenomena.

Nonlinear magnetic problems arising from ferromagnetic materials are considered and solved by applying the Newton-Raphson method. For soft ferromagnetic materials, B-H curves are used to describe the permeability, and polynomial fitting is used to construct smooth curves from experimental data. To include the hysteresis phenomenon in hard ferromagnetic materials, the Jiles-Atherton (J-A) model is introduced to characterize the nonlinear property in which an ordinary differential equation (ODE) relates the magnetic flux density with its corresponding magnetic field. The classic Runge-Kutta method is adopted to accurately solve the ODE in the J-A model.

EM and thermal variations have different timescales and the heat transfer process is far slower than electromagnetic variations. To enhance the simulation efficiency, different time-step sizes are applied. After each thermal time step, the material properties are first updated based on the temperature distribution and the EM problem is solved for several periods. When marching into the next thermal time step, the heat source is extrapolated from the EM losses to obtain the updated values, and the thermal system is solved again until a steady state is reached. Various numerical examples are presented to validate the implementation and demonstrate the accuracy, efficiency, and applications of the proposed numerical algorithms.

ACKNOWLEDGMENTS

First, I would like to express my sincere gratitude to my adviser, Professor Jian-Ming Jin, for his guidance, support, and encouragement during my M.S. study at the University of Illinois at Urbana-Champaign. Professor Jin is an excellent adviser who guided me to transit from a student to a graduate researcher. His valuable suggestions helped me gradually learn how to initiate a research project, identify and pursue the best directions, and handle challenges in the study. I have benefited greatly from his profound knowledge in the area of computational electromagnetics.

I am also very grateful to Professor Philip T. Krein for his introduction to this research topic and support. It was Professor Krein who provided me with the interesting ideas and challenging problems that are of great importance in the area of electric machinery design.

I would also like to thank the members in our group for their sincere friendship and helpful discussions. Especially, I thank Dr. Su Yan, who provided a lot of important suggestions during my first year as a graduate student, and for his outstanding work in nonlinear magnetic problems which paved a way for this research.

I am also grateful to my roommate Yunlai Chen, for the enjoyable years at Urbana. His impressive cooking always improved the quality of life and served as a good reward after a busy day. He often tried new recipes on weekends and made awesome dishes. I also thank my friends Nanjie Yu, Mingye Xiong and Hsuan-Ping Lee for the fun and relaxation we had playing Mahjong on some weekends that provided a break from our heavy workload. I really value our friendship.

TABLE OF CONTENTS

CHAPTER 1

INTRODUCTION

1.1   Background

Electrical machines play an important role in a variety of applications in industry. Among different types of electric motors, permanent magnet (PM) motors and induction motors (IM) are most popular [1-3]. Over the past decades, PM motors have been widely investigated and the designs have been optimized to achieve high performance. PM motors in general are considered to have higher efficiency than IMs [4]. However, their drawbacks are also well known. Due to the use of rare-earth permanent magnets, PM motors are more expensive. Besides, thermal limits must be enforced with care. In PM motors, the magnetic flux density is directly linked with the remnant magnetic flux in the magnets. If losses in the motor increase and the temperature rises above a certain point, the demagnetization may occur to the magnets [5]. This will not only degrade the efficiency but also cause irreversible damage to the machine.

In comparison, IMs are much cheaper and simpler. Although the efficiency is traditionally reported to be lower than that of PM motors, most commercial IMs have not been optimized to achieve their best performance [6]. In recent studies [7-10], if the IM is carefully designed to operate at its optimal condition, the efficiency is comparable with that of PM motors. Therefore, it is of great interest to model and evaluate IMs to facilitate high-performance designs.

In order to predict and evaluate the performance of IMs, an accurate modeling is required. Since the finite element method (FEM) is a powerful numerical method with the capability of modeling complex geometries [11], it can achieve a great balance between accuracy and cost when compared with analytical methods [12-14], and thus is used as the primary approach to analyze the design. However, several challenges need to be addressed. In IMs, the cores are typically made of ferromagnetic materials to offer a high permeability which usually exhibit nonlinear properties, i.e. the permeability is a function of magnetic fields. Therefore, the ability of solving nonlinear magnetic problems must be incorporated into the FEM solver.

Meanwhile, EM fields will generate losses, such as the Joule losses and the magnetic core losses, which will result in a temperature increase in the machine and affect its efficiency. The temperature

increase, in turn, will change the material properties. It is essential to perform a fully coupled EM-thermal co-simulation to accurately evaluate the performance.

1.2   Time Domain Finite Element Method

To model the electric machines and analyze their performance, different techniques can be employed, among which the full-wave simulation tools are more accurate as they solve Maxwell's equations directly and compute the electromagnetic field distribution in the machine. Three popular numerical methods have been developed during the past decades, the method of moment (MoM) [15, 16], the finite-difference time-domain (FDTD) [17, 18] and the finite element method (FEM). They all transform Maxwell's equations with boundary values into the corresponding linear systems of equations that can be solved numerically.

The MoM uses the Green functions to calculate the scattered field from the surface charge or surface current on the conductors, which accurately accounts for the radiation condition. The number of unknowns from MoM is typically small because only the surface of objects is discretized, but the resulting impedance matrix is full, and the computational cost is high. Moreover, the Green functions have to be formulated for each specific problem, and it could be extremely complicated or even impossible for problems with complex structures. The FDTD method is easy to formulate and the time marching process is straightforward. There is no need to assemble a global matrix and solve the linear systems of equations, which gives little computation load. However, the mesh that discretizes the objects usually uses cubes which cannot model complex shapes accurately.

The FEM solves the partial differential form of Maxwell's equations. After discretizing the complex geometry using tetrahedra, the electromagnetic fields are expanded using basis functions defined in each element, and a global matrix system is assembled by applying Galerkin's method. It is very powerful when modeling complex geometries and material compositions. The FEM itself can be formulated in both frequency and time domains. When nonlinear problems are encountered, such as nonlinear permeability or nonlinear conductivity, where the material properties depend on the fields, the time domain FEM (TDFEM) will be an appropriate approach. An extremely important advantage of the TDFEM is that it can be formulated to be unconditionally stable by

utilizing the Newmark-β scheme [19]. The time-step size does not need to be reduced even when very small elements are present, and can be chosen to be a large value as long as it can capture the time variation of the fields. This is significant when the frequency is low and the geometry has fine structures.

1.3   Modeling of Nonlinear Magnetic Materials

Ferromagnetic compounds are widely used in electric machines. Those materials exhibit nonlinear behaviors where the permeability is a function of the magnetic field density. To accurately analyze the machines and achieve optimal device performance, the nonlinear properties of the ferromagnetic materials must be modeled properly in the design process.

The nonlinear behaviors are usually described by two types, the B-H curve where the magnetic flux density (B field) is a single-value function of the magnetic field density (H field), and the hysteresis model where the B field and the H field form a loop. The B-H curve can be simply characterized by polynomial interpolation from measured data. With a B-H curve, the B field as well as the permeability is easily calculated from the H field. The modeling of the hysteresis behavior, however, is more involved. Different models have been developed during the past years, among which the Preisach model and the Jiles-Atherton (J-A) model are commonly used [20-23]. In this work the J-A model is adopted because it can be easily incorporated into the TDFEM. The J-A model is expressed by an ordinary differential equation (ODE) which can be solved by using the classic Runge-Kutta method.

1.4   EM-Thermal Co-Simulation

In the literature [24-30], EM-thermal modeling has been studied to predict the performance of motors by considering the coupling between EM losses and thermal effects on material properties. However, in those sources, either an equivalent EM/thermal lumped model is employed, or the full-wave EM analysis is conducted in the frequency domain. As such, nonlinear magnetic effects are difficult to include in these models, and thus the analysis is not accurate when the system is

3

sensitive to temperature change. In this work, the EM field distribution and heat transfer are computed in the time domain.

In the TDFEM formulation for the EM part, although the Newmark-β method is applied due to its unconditional stability, the time step is still restricted by the frequency of the fields, namely the time step should be fine enough to capture the time variation of the electric and magnetic fields. Usually, Δt is chosen to be one 20th of the period of the excitation. In most applications in electrical machinery designs where the frequency can be as low as 50Hz, the EM variation cycles are on the order of milliseconds. However, for the thermal analysis, the temperature change rate is usually on the order of seconds to minutes, which is far larger than that of the EM field. To efficiently couple these two processes, different time-step sizes are chosen, and within each thermal step, extrapolation is applied to predict the EM losses.

CHAPTER 2

MODELING OF NONLINEAR MAGNETIC PROBLEMS

2.1 Introduction

In this chapter, the formulation of the TDFEM is presented. There are generally two approaches to formulate the FEM in the time domain. The first approach solves two time-dependent first-order Maxwell's equations, i.e. Ampere's and Faraday's laws. The partial derivative with respect to time is discretized through central differencing. The resulting system is conditionally stable in the sense that the time-step size is limited by the finest size of the elements. Moreover, both electric and magnetic fields are expanded using basis functions, and the degree of freedom is twice larger than the formulation that solves only either electric or magnetic field.

The second approach is based on the second-order wave equation where the electric field is usually to be solved. The time derivative can be approximated by adopting backward differencing, which is unconditionally stable but only has first-order accuracy. The accuracy can be improved by using central differencing. However, the resulting conditional stability is not preferred for the low frequency problems, because the period is much larger than the time-step size and one has to solve thousands of steps per period, which is impossible in practice. The well-known Newmark-β time integration theme can achieve unconditional stability and second-order accuracy when $\beta \geq \frac{1}{4}$. Therefore, the choice of the time-step size is independent of the mesh size.

To model nonlinear materials, the nonlinear TDFEM is formulated based on the widely used numerical method for solving nonlinear equations, the Newton-Raphson method [31], due to its quadratic convergence. The following sections will give detailed formulations, and numerical examples are shown to investigate the performance.

2.2 Time Domain Finite Element Method for Linear Problems

First, we start from Maxwell's equations in the time domain

$$\nabla \times \mathbf{E} = -\frac{\partial \mathbf{B}}{\partial t} \tag{1}$$

$$\nabla \times \mathbf{H} = \frac{\partial \mathbf{D}}{\partial t} + \sigma \mathbf{E} + \mathbf{J}_{imp} \tag{2}$$

By using the magnetic vector potential

$$\nabla \times \mathbf{A} = \mathbf{B} \tag{3}$$

$$\mathbf{E} = -\frac{\partial \mathbf{A}}{\partial t} \tag{4}$$

one obtains the second-order curl-curl equation

$$\nabla \times (\nu_r \nabla \times \mathbf{A}) + \frac{\varepsilon_r}{c_0^2} \frac{\partial^2}{\partial t^2} \mathbf{A} + \sigma \frac{\eta_0}{c_0} \frac{\partial}{\partial t} \mathbf{A} = \mu_0 \mathbf{J}_{imp} \tag{5}$$

where $\nu_r = 1/\mu_r$ and ε_r are the relative reluctivity and permittivity of the material, $\eta_0 = \sqrt{\mu_0/\varepsilon_0}$ and c_0 are the intrinsic impedance and the speed of light in free space, respectively. $\mathbf{J}_{imp}$ is the impressed current density. To discretize the equation, the magnetic vector potential is first expanded in terms of vector basis functions

$$\mathbf{A} = \sum_{j}^{N} a_j \mathbf{N}_j \tag{6}$$

Here the curl-conforming basis functions are adopted. Applying Galerkin's method, (5) is tested and converted into a matrix equation

$$[M]\frac{\partial^2}{\partial t^2}\{a\} + c_0 \eta_0 [G]\frac{\partial}{\partial t}\{a\} + c_0^2 [S]\{a\} = \mu_0 \{b\} \tag{7}$$

where

$$M_{ij} = \iiint_V \varepsilon_r \mathbf{N}_i \cdot \mathbf{N}_j dV \tag{8}$$

$$G_{ij} = \iiint_V \sigma \mathbf{N}_i \cdot \mathbf{N}_j dV \tag{9}$$

$$S_{ij} = \iiint_V \nu_r \left(\nabla \times \mathbf{N}_i\right) \cdot \left(\nabla \times \mathbf{N}_j\right) dV \tag{10}$$

$$b_i = \iiint_V \mathbf{N}_i \cdot \mathbf{J}_{imp} \, dV \tag{11}$$

In the above expression, the homogeneous Dirichlet boundary condition or the perfectly electrical conductor (PEC) boundary condition is applied. To fully discretize (7) in time, the Newmark-β method is employed, and the resulting system is unconditionally stable and second-order accurate when choosing $\beta = 1/4$.

In the Newmark-β method, the time derivatives are approximated by the central difference, whereas the time dependent variable is approximated by the weighted sum of its values at three consecutive time steps:

$$g(t) = \beta g^{n+1} + (1 - 2\beta) g^n + \beta g^{n-1}$$
$$\frac{d}{dt} g(t) = \frac{1}{2\Delta t} \left(g^{n+1} - g^{n-1} \right) \tag{12}$$
$$\frac{d^2}{dt^2} g(t) = \frac{1}{\Delta t^2} \left(g^{n+1} - 2g^n + g^{n-1} \right)$$

Application of the Newmark-β method to (7) yields the fully discrete system (with β = 1/4)

$$[K^0]\{a\}^{n+1} = \{\tilde{b}\}^n + [K^1]\{a\}^n + [K^2]\{a\}^{n-1} \tag{13}$$

with

$$[K^0] = [M] + \frac{1}{2}\eta_0 c_0 \Delta t [G] + \frac{1}{4}c_0^2 \Delta t^2 [S] \tag{14}$$

$$[K^1] = 2[M] - \frac{1}{2}c_0^2 \Delta t^2 [S] \tag{15}$$

$$[K^2] = -[M] + \frac{1}{2}\eta_0 c_0 \Delta t [G] - \frac{1}{4}c_0^2 \Delta t^2 [S] \tag{16}$$

$$\{\tilde{b}\} = \eta_0 c_0 \Delta t^2 \left(\frac{1}{4}\{b\}^{n+1} + \frac{1}{2}\{b\}^n + \frac{1}{4}\{b\}^{n-1} \right) \tag{17}$$

For the $(n+1)^{th}$ time step, the system can be solved from the solutions at the $(n-1)^{th}$ and the nth time steps. Once $\{a\}$ is solved, the electric field $\mathbf{E}$ and the magnetic field $\mathbf{H}$ can be recovered.

2.3   Newton-Raphson Method for Nonlinear TDFEM

To model the nonlinear magnetic problems, the nonlinear TDFEM based on the Newton-Raphson method is derived. The magnetic field is separated into the linear and nonlinear parts

$$\mathbf{H} = \nu_r \nu_0 \mathbf{B} = \nu_r^{opt} \nu_0 \mathbf{B} + \mathbf{R} = \nu_r^{opt} \nu_0 \nabla \times \mathbf{A} + \mathbf{R}(\mathbf{A}) \tag{18}$$

where ν_r^{opt} is a constant, and the nonlinearity occurs in the term $\mathbf{R}$. In this case, (5) becomes

$$\nabla \times \left[\nu_r^{opt} \nabla \times \mathbf{A} + \mu_0 \mathbf{R}(\mathbf{A}) \right] + \frac{\varepsilon_r}{c_0^2} \frac{\partial^2}{\partial t^2} \mathbf{A} + \sigma \frac{\eta_0}{c_0} \frac{\partial}{\partial t} \mathbf{A} = \mu_0 \mathbf{J}_{imp} \tag{19}$$

Following the same procedure, the discretized matrix equation can be obtained:

$$[\tilde{K}^0]\{a\}^{n+1} + \{R\} = \{\tilde{b}\}^n + [\tilde{K}^1]\{a\}^n + [\tilde{K}^2]\{a\}^{n-1} \tag{20}$$

where the $[K]$ matrices have the same form as (13)~(15), except that the $[S]$ matrix is now defined as

$$\tilde{S}_{ij} = \iiint_V \nu_r^{opt} \left(\nabla \times \mathbf{N}_i \right) \cdot \left(\nabla \times \mathbf{N}_j \right) dV \tag{21}$$

with

$$R_i = \mu_0 c_0^2 \Delta t^2 \iiint_V \mathbf{N}_i \cdot (\nabla \times \mathbf{R}) dV = \mu_0 c_0^2 \Delta t^2 \iiint_V \nabla \times \mathbf{N}_i \cdot \mathbf{R} dV \tag{22}$$

For a nonlinear problem

$$\mathbf{f}(\mathbf{x}) = 0 \tag{23}$$

the solution can be calculated iteratively by applying the Newton-Raphson method

$$\mathbf{x}_{k+1} = \mathbf{x}_k - \mathbf{J}^{-1}(\mathbf{x}_k)\mathbf{f}(\mathbf{x}_k) \tag{24}$$

where $[\mathbf{J}]$ is the Jacobian matrix defined as

$$J_{ij} = \frac{\partial f_i}{\partial x_j} \tag{25}$$

Back to the EM problem (19), the nonlinear function can be expressed by

$$\{f\} = [\tilde{K}^0]\{a\}^{n+1} - [\tilde{K}^1]\{a\}^n - [\tilde{K}^2]\{a\}^{n-1} + \{R\} - \{\tilde{b}\}^n \tag{26}$$

Substituting into the definition, the Jacobian matrix becomes

$$J_{ij} = \frac{\partial f_i}{\partial a_j^{n+1}} = \tilde{K}_{ij}^0 + \frac{\partial R_i}{\partial a_j^{n+1}} \tag{27}$$

Note that from (17) the nonlinear part of the magnetic field can be written as

$$\mathbf{R} = \left(\nu_r - \nu_r^{opt}\right)\nu_0\mathbf{B} \tag{28}$$

Therefore, it can be obtained that

$$
\begin{aligned}
\frac{\partial \mathbf{R}}{\partial a_j^{n+1}} &= \frac{\partial}{\partial a_j^{n+1}}\left[\left(\nu_r - \nu_r^{opt}\right)\nu_0\mathbf{B}\right] \\
&= \frac{\partial \nu_r}{\partial a_j^{n+1}}\nu_0\mathbf{B} + \left(\nu_r - \nu_r^{opt}\right)\nu_0\frac{\partial \mathbf{B}}{\partial a_j^{n+1}} \\
&= \frac{\partial \nu_r}{\partial B}\frac{\partial B}{\partial a_j^{n+1}}\nu_0\mathbf{B} + \left(\nu_r - \nu_r^{opt}\right)\nu_0\frac{\partial \mathbf{B}}{\partial a_j^{n+1}}
\end{aligned}
\tag{29}
$$

Because the magnetic field is expanded by

$$\mathbf{B} = \nabla \times \mathbf{A} = \sum_j \left(\frac{1}{4}a_j^{n+1} + \frac{1}{2}a_j^n + \frac{1}{4}a_j^{n-1}\right)\nabla \times \mathbf{N}_j \tag{30}$$

we obtain

$$
\begin{aligned}
\frac{\partial \mathbf{B}}{\partial a_j^{n+1}} &= \frac{1}{4}\nabla \times \mathbf{N}_j \\
\frac{\partial B}{\partial a_j^{n+1}} &= \frac{1}{4}\nabla \times \mathbf{N}_j \cdot \frac{\mathbf{B}}{B}
\end{aligned}
\tag{31}
$$

We also have

$$\frac{\partial \nu_r}{\partial B} = \frac{\partial}{\partial B}\left(\frac{\mu_0 H}{B}\right) = \frac{1}{B}\left(\nu_r^d - \nu_r\right) \tag{32}$$

9

where $v_r^d = \dfrac{\partial}{\partial B}(\mu_0 H)$ is the relative differential reluctivity.

Substituting (31) and (32) into (29), we obtain

$$\begin{aligned}
\frac{\partial \mathbf{R}}{\partial a_j^{n+1}} &= \frac{1}{4} v_0 \left(v_r^d - v_r \right) \frac{\mathbf{B}}{B} \left[\left(\nabla \times \mathbf{N}_j \right) \cdot \frac{\mathbf{B}}{B} \right] \\
&\quad + \frac{1}{4} v_0 \left(v_r - v_r^{opt} \right) \left(\nabla \times \mathbf{N}_j \right)
\end{aligned} \tag{33}$$

From (22), (27) and (33), the Jacobian matrix can finally be derived as

$$\begin{aligned}
J_{ij} &= \tilde{K}_{ij}^0 + \frac{\partial R_i}{\partial a_j^{n+1}} \\
&= \tilde{K}_{ij}^0 + \frac{1}{4} c_0^2 \Delta t^2 \iiint_V \left(v_r^d - v_r \right) \left[\left(\nabla \times \mathbf{N}_i \right) \cdot \frac{\mathbf{B}}{B} \right] \left[\left(\nabla \times \mathbf{N}_j \right) \cdot \frac{\mathbf{B}}{B} \right] dV \\
&\quad + \frac{1}{4} c_0^2 \Delta t^2 \iiint_V \left(v_r - v_r^{opt} \right) \left(\nabla \times \mathbf{N}_i \right) \cdot \left(\nabla \times \mathbf{N}_j \right) dV
\end{aligned} \tag{34}$$

2.4 B-H Relation for the Ferromagnetic Materials

Ferromagnetic materials have been widely used in the machines as they have very high permeabilities, e.g., as high as 10^6. When a field is applied, the materials are magnetized, and the magnetic flux density is increased as the external field becomes larger. However, when the applied field is removed or the direction of the applied field changes, the residual magnetism cannot disappear immediately, which exhibits the hysteresis loop, as shown in Figure 2.1. The magnetic hysteresis results in the dissipation of energy in the form of heat. Given different properties of the materials, they are characterized as soft ferromagnetic materials with narrow loops and hard ferromagnetic materials with wide loops.

For the soft ferromagnetic materials, the magnetic losses are usually small, and the B-H relation is characterized as the B-H curve, where the losses are ignored. For the hard ferromagnetic materials, the hysteresis loop must be considered, and the Jiles-Atherton (J-A) model is adopted.
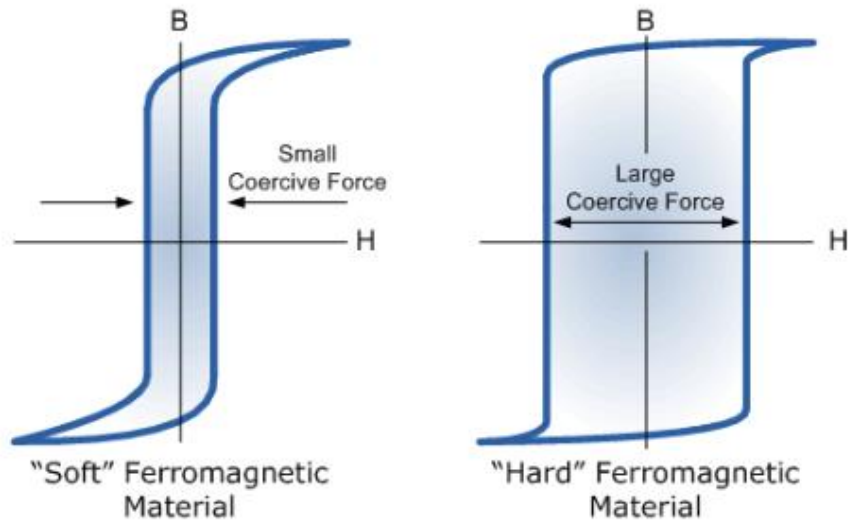
Figure 2.1 Hysteresis loop for ferromagnetic materials.

2.4.1 Soft Ferromagnetic Materials and B-H Curve

For the soft ferromagnetic materials, the B-H relations are described by the B-H curve. Usually the material properties are measured at discrete points. From the available data, the B-H curve can be approximated using the cubic spline interpolation:

$$B = aH^3 + bH^2 + cH + d \tag{35}$$

where the coefficients a, b, c, d are to be determined. In the Newton-Raphson method, not only the $|\mathbf{B}|$ and $|\mathbf{H}|$, but also the relative differential permeability v_r^d are needed. The cubic spline interpolation is chosen since first and second derivatives are continuous. As an example, Figure 2.2 shows the measured B-H data and its interpolated curve.

However, in practice, the magnetic flux density B is known and the magnetic field density H is to be calculated. Therefore, instead of the B-H relation, the H-B curve is used. The relation is appoximated by

$$H = \tilde{a}B^3 + \tilde{b}B^2 + \tilde{c}B + \tilde{d} \tag{36}$$
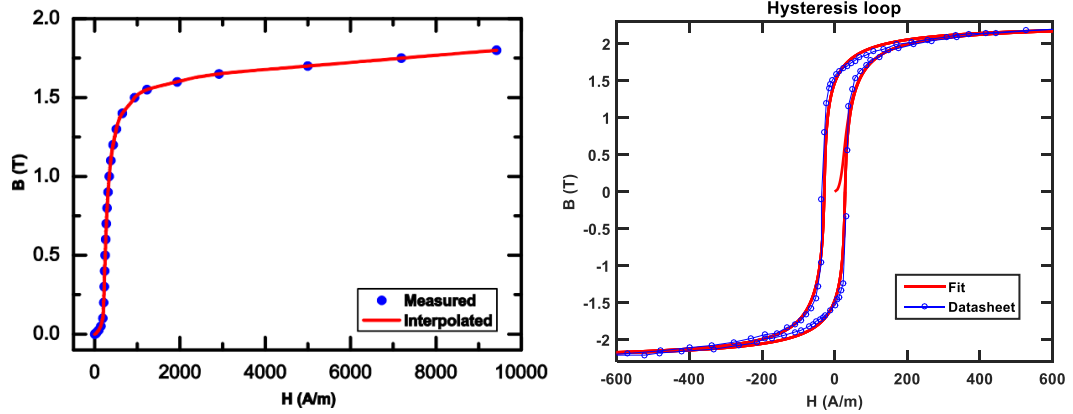
11

Figure 2.2 An example of the B-H relation. Left: B-H curve for soft materials; Right: hysteresis loop for hard materials.

For the H-B curve interpolated from (36), the relative differential permeability v_r^d has an analytical expression which is given by

$$v_r^d = \frac{\partial}{\partial B}\left(\mu_0 H\right) = 3\mu_0 \tilde{a} B^2 + 2\mu_0 \tilde{b} B + \tilde{c}\mu_0 \tag{37}$$

At each Newton-Raphson iteration, the magnetic flux density B is first calculated from the vector potential A, and then the magnetic field density H as well as the relative differential permeability v_r^d is obtained from (36) and (37). The Jacobian matrix is available by substituting those values into (34) and the unknowns can be updated.

2.4.2   Hard Ferromagnetic Materials and Hysteresis Loop

For the hard ferromagnetic materials, the hysteresis loop must be modeled to account for the magnetic losses in order to accurately evaluate the performance of machines. In this work, the J-A model is applied. In the J-A model, the total magnetization is characterized by a differential relation as

$$dM = \chi^d dH \tag{38}$$

where the differential susceptibility is given by

12

$$\chi^d = \begin{cases} \dfrac{(M_{an}-M)/k_p\delta+c\varsigma}{1-\alpha\left[(M_{an}-M)/k_p\delta+c\varsigma\right]}, & when\ (M_{an}-M)dH_e > 0 \\[4ex] \dfrac{c\varsigma}{1-\alpha c\varsigma}, & when\ (M_{an}-M)dH_e \leq 0 \end{cases} \tag{39}$$

In (39), the anhysteretic magnetization M_{an} is described by

$$M_{an} = M_s\left[\coth\left(\frac{H_e}{a}\right)-\frac{a}{H_e}\right] \tag{40}$$

and the effective field H_e is defined as

$$H_e = H + \alpha M \tag{41}$$

In the above expressions, M_s, a, α, c, k_p are the coefficients that characterize the hysteresis loop in the J-A model.

Since the constitutive relation is now described as an ODE, it can be solved with high accuracy by employing the Runge-Kutta method. In Figure 2.2, an example of the hysteresis loop is fitted from the measured data by using the J-A model.

2.5 Numerical Examples

In this section, several examples are shown to demonstrate the capability for modeling the nonlinear magnetic problems. These examples are selected from the benchmark problems from the "testing electromagnetic analysis methods" (TEAM) workshop [32] and they cover both the soft and hard ferromagnetic materials. Note that all the examples are simulated in the time domain, and the fields which are plotted along a sampling line are obtained by performing the Fourier transform and selecting values at the frequency of the excitation.

2.5.1 TEAM Problem 21b

The TEAM problem 21b-MN is considered. The problem consists of two excited coils placed over two plates, of which one is made of non-magnetic steel and the other is made of magnetic steel. The geometry as well as the dimensions of the problem are shown in Figure 2.3. The number of turns for each coil is 300, and the exciting current is 10A with the frequency of 50Hz. The non-magnetic steel has the conductivity of $\sigma = 1.3889 \times 10^6 \ S/m$ with the relative permeability $\mu_r = 1$; the magnetic steel has the conductivity of $\sigma = 6.484 \times 10^6 \ S/m$ and the relative permeability is given by the B-H curve shown in Figure 2.4. The x-components of the magnetic field along two observation lines are plotted compared with the measurements in Figure 2.5. The simulated results agree with the measurement very well. Note that the half-order (or incomplete first-order) basis functions are utilized to expand the magnetic vector potential. If higher order basis functions are employed, the simulation results are expected to be smoother in the spatial distribution.
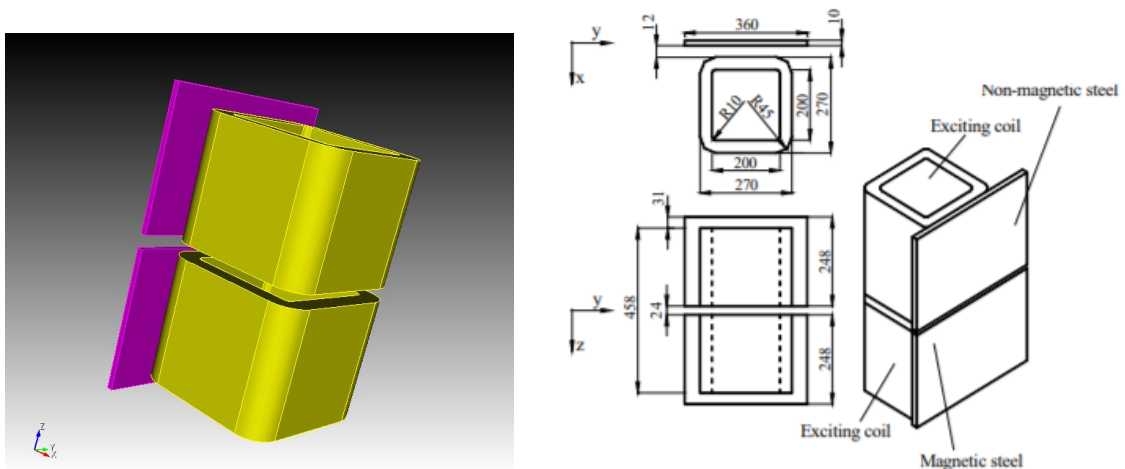
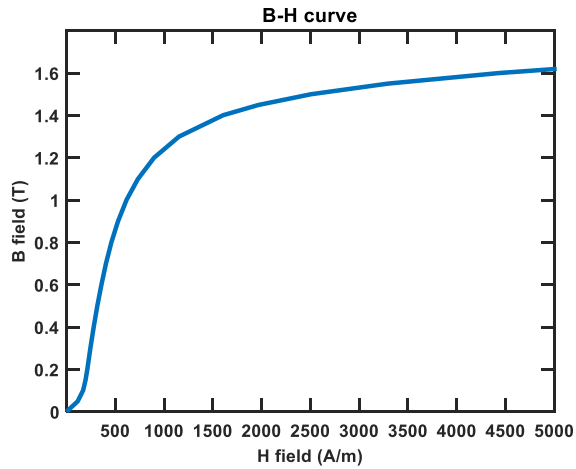*Figure 2.3 Geometry and dimensions of TEAM problem 21b.*

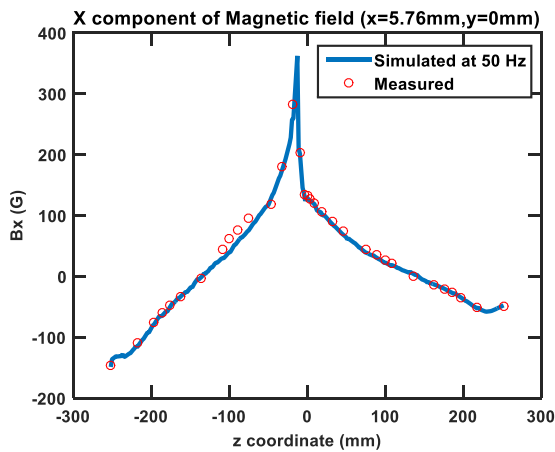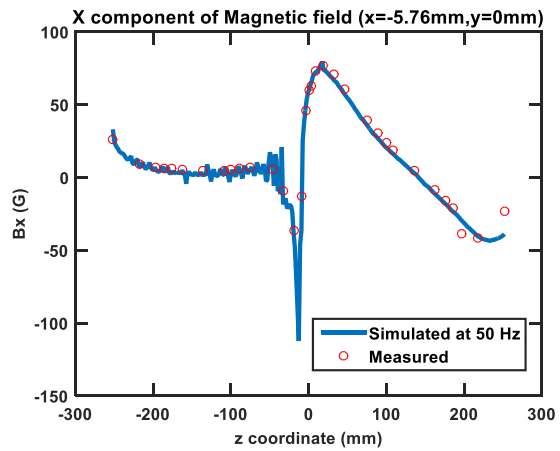*Figure 2.4 Constitutive relation for TEAM problem 21b.*

Figure 2.5 X-components of the magnetic field along two observation lines. Top: line located at x = -5.76mm and y = 0.0mm; Bottom: line located at x = 5.76mm and y = 0.0mm.

15

2.5.2   TEAM Problem 32

A test case for the validation of magnetic field analysis with a hysteresis model is considered. The case is from the TEAM problem 32, which is a three-limbed ferromagnetic core shown in Figure 2.6. The core is 0.48mm thick and has conductivity $\sigma = 1.78\,MS/m$. Two windings of 90 turns are placed on the external two limbs. In the test, both coils are excited by a sinusoidal current of 1.15A at a frequency of 10Hz. The ferromagnetic material is modeled by the J-A model, and the parameters in the model are chosen as $M_s = 1.168 \times 10^6\,A/m$, $a = 60\,A/m$, $\alpha = 10^{-4}$, $c = 0.2$ and $k_p = 130\,A/m$. Figure 2.7 shows the hysteresis loop with measurement and fitted curve. The magnetic flux densities are recorded as a function of time at two points on both the left and central limbs, as shown in Figure 2.8. Good agreement is observed. The field distribution in space is also given at time = 5ms.
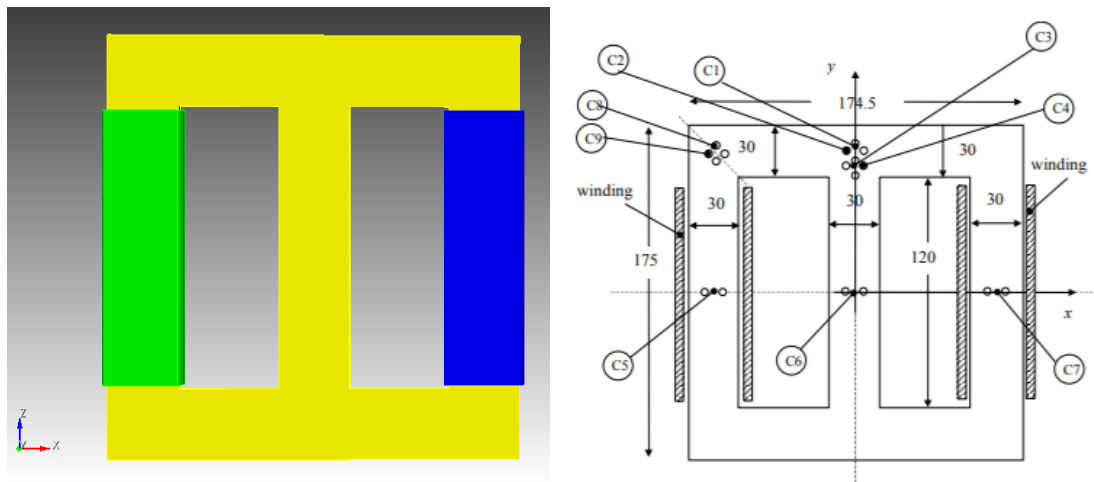

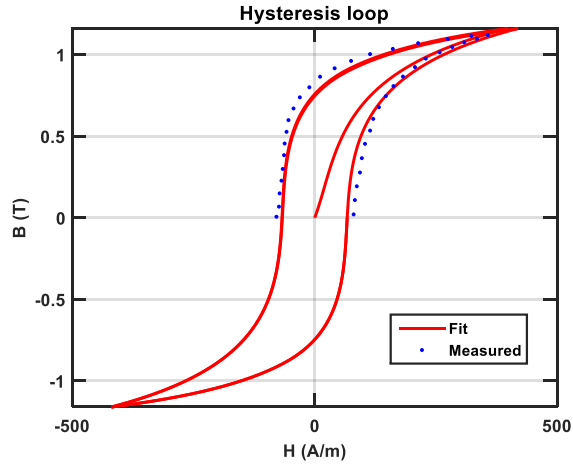*Figure 2.6 Geometry and dimensions of TEAM problem 32.*

16

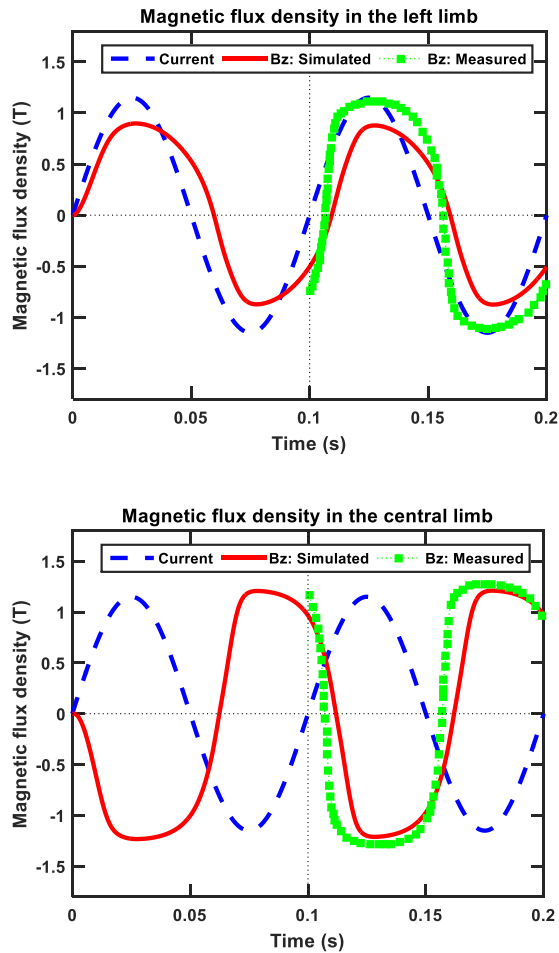*Figure 2.7 Hysteresis loop of the core material in TEAM problem 32.*

Figure 2.8 Simulated results for TEAM problem 32. Top: z-component of magnetic flux density versus time at the center of the left limb; Bottom: z-component of magnetic flux density versus time at the center of the central limb.

2.5.3　　　Axial Air Gap Induction Motor

In this section, an induction motor example is presented to demonstrate the capability of applying the proposed method to practical applications. The induction motor considered has an axial air gap and a flat disk rotor, as shown in Figure 2.9. Detailed configuration of the motor can be found in [33].

This type of induction motor can achieve high utilization of the active materials and thus high power density, compared with conventional induction machines. A complete numerical modeling is required to accurately evaluate the performance. In most cases, the torque running at different speeds is the quantity of interest. Therefore, the machine must be explored over a wide range of speeds, and the effects of mechanical movements have to be taken into account. For the disk rotor in this example, due to the invariance along the rotating direction, the motion effect can be easily incorporated into the EM simulation by simply modifying Maxwell's equations to include the Lorentz term $\mathbf{v} \times \mathbf{B}$, where $\mathbf{v}$ is the velocity. To compute the torque, the Maxwell stress tensor [34, 35] method is employed.

To drive the motor, three-phase currents are excited at 50Hz with a magnitude of 2A, as shown in Figure 2.10. The number of turns for each coil is 290. Figure 2.11 presents time variation of the torques under different speeds, and Figure 2.12 gives a comparison of the average torque between the full-wave simulation and experimental data.
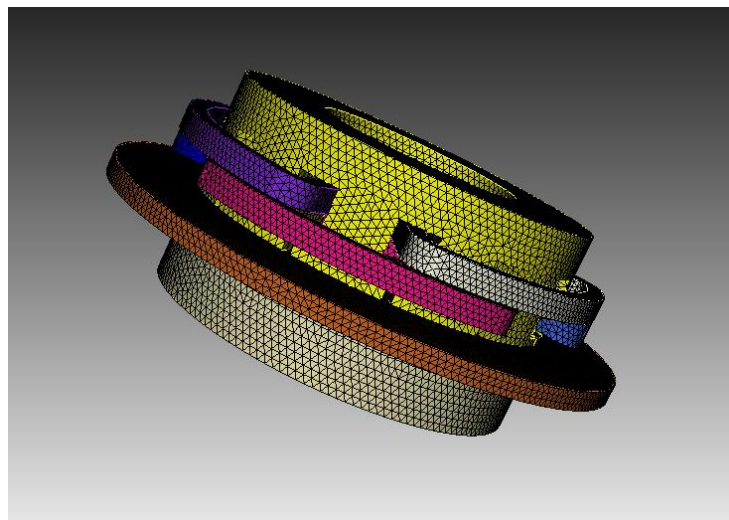

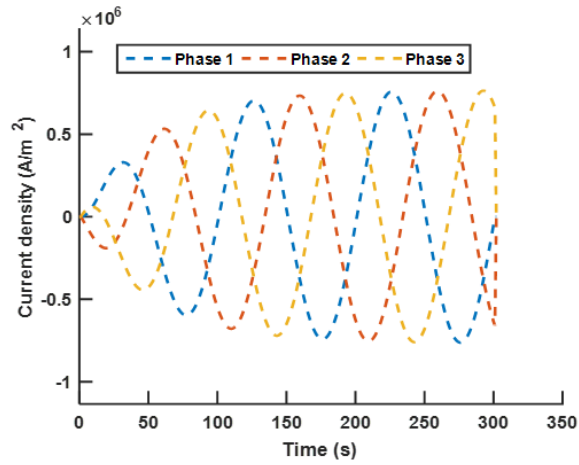*Figure 2.9 Geometry of the axial air gap induction motor.*
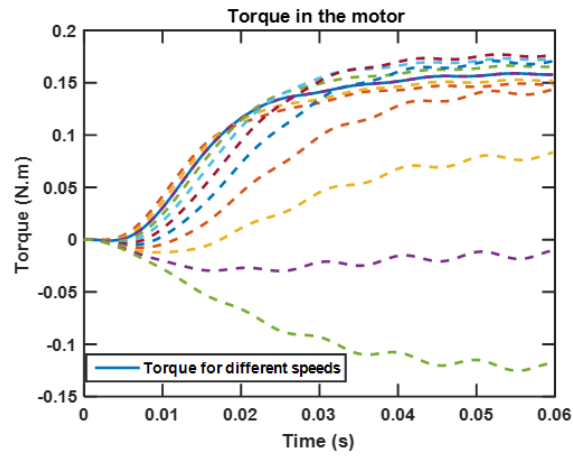
Figure 2.10 Three-phase current excitation.
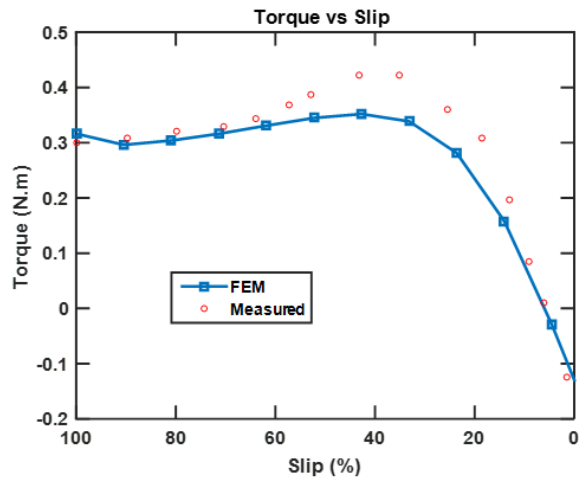

Figure 2.11 Torque versus time at different speeds.

Figure 2.12 Comparison of the predicted torque between full-wave simulation and experiment.

CHAPTER 3

FRAMEWORK FOR EM-THERMAL CO-SIMULATION

3.1 Introduction

In this chapter, an efficient framework for the EM-thermal co-simulation is proposed. In the machinery design, the thermal effect must be considered because it affects the performance of the machine. First, the losses, including the coil losses, copper losses and magnetic core loss, will waste power and decrease the efficiency of the design. Second, the losses are dissipated in the form of heat, and the increased temperature will change the material properties. More seriously, when the temperature increases to a certain point, i.e. the Curie point, the magnetic core will be completely demagnetized [36, 37], causing irreversible damages to the machine. To fully understand the behavior of the machine, the EM-thermal co-simulation is required. In the following sections, the framework for coupling the EM and thermal solvers is developed and several numerical examples are presented to demonstrate the capability of the proposed method.

3.2 Heat Transfer Equation and Thermal Solver

The governing equation for the transient heat conduction is

$$\rho C_p \frac{\partial T}{\partial t} = \nabla \cdot \kappa \nabla T + \dot{q} \tag{42}$$

where ρ is the density of the materials, C_p is the specific heat, κ is the thermal conductivity, and $\dot{q}$ is the volumetric heat source. The corresponding boundary conditions commonly used in the thermal analysis are the heat flux boundary

$$\hat{n} \cdot \kappa \nabla T = -q_s \tag{43}$$

as well as the convective boundary

$$\hat{n} \cdot \kappa \nabla T = -h(T - T_a) \tag{44}$$

where q_s is the heat flux density, h is the convective coefficient and T_a is the ambient temperature.

Applying Galerkin's method to (42), one obtains the semi-discrete matrix equation

$$[C_T]\frac{\partial}{\partial t}\{T\}+[K_T]\{T\}=\{Q_T\} \tag{45}$$

where

$$[C_T]_{ij}=\iiint_V \rho C_p N_i N_j dV \tag{46}$$

$$[K_T]_{ij}=\iiint_V \kappa \nabla N_i \cdot \nabla N_j dV+\iint_S hN_i N_j dS \tag{47}$$

$$\{Q_T\}_i=\iiint_V N_i \dot{q} dV+\iint_S hN_i T_a dS \tag{48}$$

In the above equations, the surface integrals come from the convective boundary condition, and N_i represents nodal scalar basis functions such that

$$T=\sum_j N_j T_j \tag{49}$$

To discretize (45) in time, the backward difference is used

$$[C_T]\frac{\{T\}^n-\{T\}^{n-1}}{\Delta t}+[K_T]\{T\}^n=\{Q_T\}^n \tag{50}$$

which yields the time-marching scheme

$$\left([C_T]+\Delta t[K_T]\right)\{T\}^n=[C_T]\{T\}^{n-1}+\Delta t\{Q_T\}^n \tag{51}$$

3.3   EM-Thermal Coupling

The coupling between the EM and thermal analyses may look straightforward by solving Maxwell's and heat transfer equations simultaneously. They are coupled through the dissipated power and the temperature-dependent material properties. However, in the physical process, the

two processes have different timescales, and the temperature change is much slower than the EM field variation. To be specific, the EM variation cycles are usually on the order of milliseconds to seconds, whereas the temperature change rate is on the order of minutes. Performing the two simulations together at the same time step is too expensive.

One solution is to apply different time-step sizes to different processes. During one thermal cycle, the EM problem is first solved for several periods, and the losses are calculated. When marching into the next thermal cycle, the heat source at the current time step is extrapolated from the losses obtained previously, and the thermal system is solved. The thermal stepping can be continued until the material properties vary significantly, for example five percent, due to the temperature change. Then the EM solver is invoked again, and the above procedure repeats. The flow chart for the whole procedure is shown in Figure 3.1.
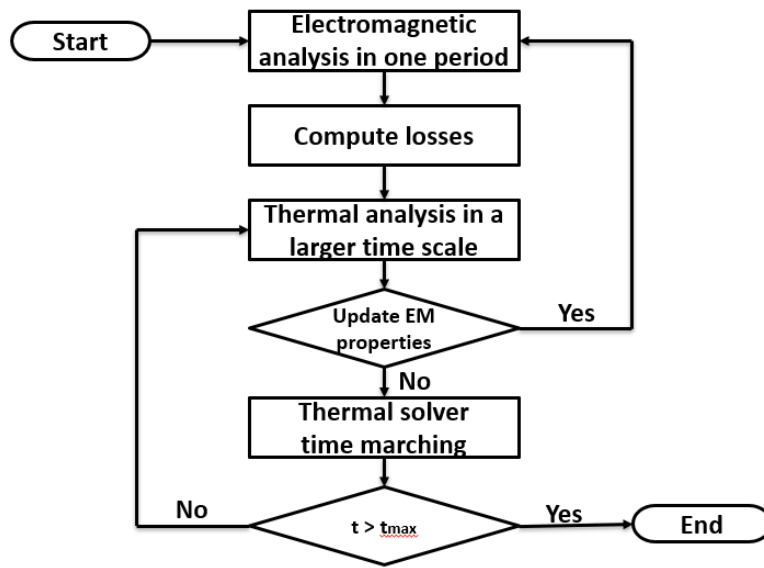

Figure 3.1 Flow chart of the EM-thermal coupling process.

3.4   Numerical Examples

In this section, several numerical examples are presented to demonstrate the capability of the proposed method.

3.4.1 Heat Transfer on IC Package

In the first example, the thermal analysis is carried out on a high-power IC package as shown in Figure 3.2. The components are modeled by five-layered substrates including the die, TIM1 (Thermal Interface Material), lid, TIM1 and the heat sink base. The dimensions and the material properties are given in Tables 3.1 and 3.2, respectively. The ambient and initial temperatures are set to 273.15K. A power of 1W is applied to the top surface of the die which is in contact with the TIM. Therefore, a surface heat flux is applied on the top surface of the die, and the value equals $5917.1598W/m^2$. The cooling effect of the heat sink is represented by the convective boundary condition which is applied to the top surface of the heat sink base with a convective coefficient equal to $20000W/m^2K$. The temperature distribution is reported in Figure 3.3 as well as the transient temperature change versus time.
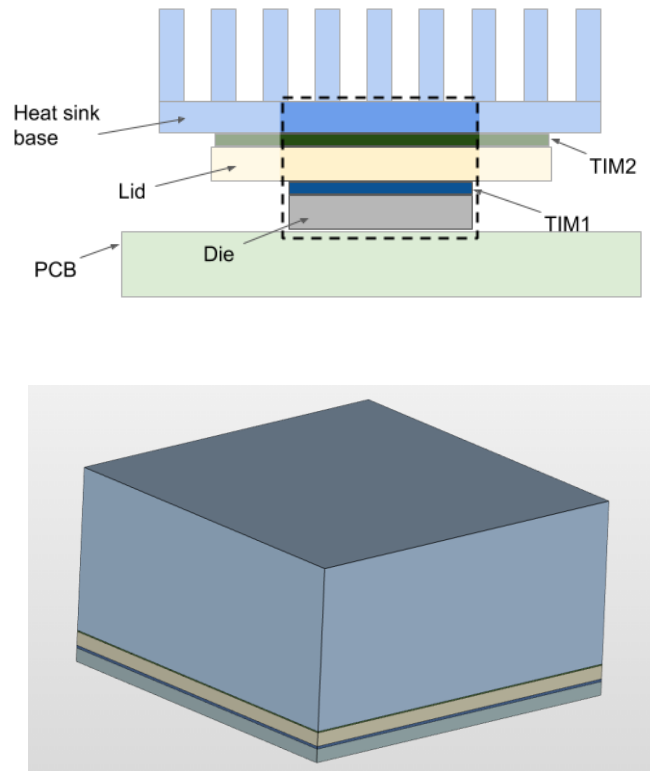

Figure 3.2 Geometry and simplified model in the IC package simulation.

Table 3.1 Dimensions of components in the IC package

Component	Length(mm)	Width(mm)	Thickness(mm)
Die	13	13	0.50
TIM1	13	13	0.10
Lid	13	13	0.50
TIM2	13	13	0.05
Heat sink base	13	13	6.00

Table 3.2 Material properties of the components in the IC package

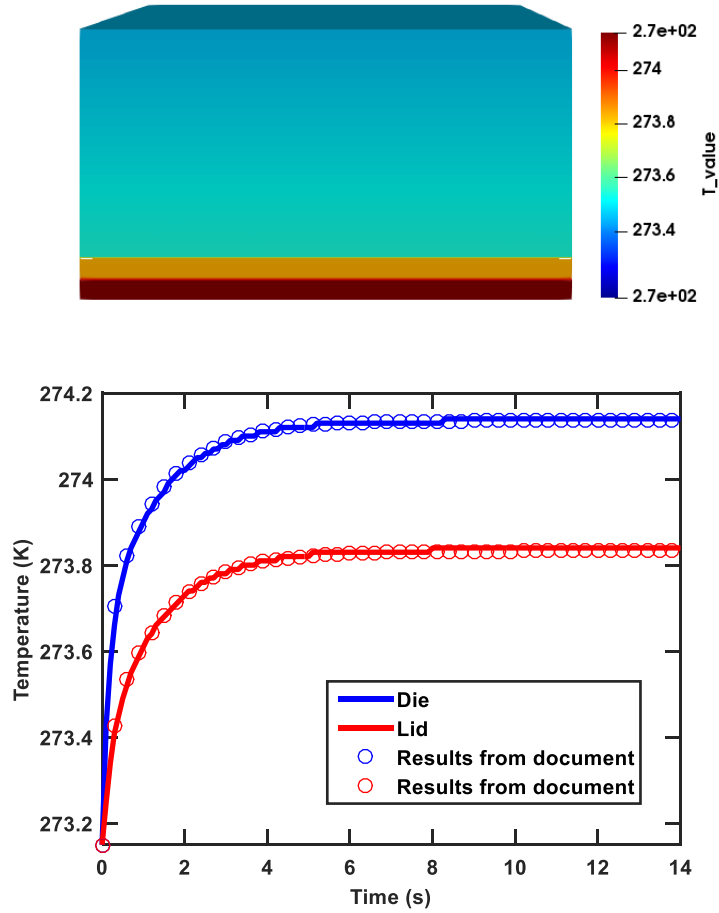| Component	Thermal conductivity (W/mK)	Density (kg/m^3)	Specific heat (J/kgK)
Die	111	2330	668
TIM1	2.0	4400	400
Lid	390	8890	385
TIM2	1.0	2500	900
Heat sink base	390	8890	385

Figure 3.3 Top: Temperature distribution; Bottom: Temperature change versus time in the Die and Lid regions; (reference results from [44]).

3.4.2   Induction Heating Problem 1

The induction heating problem [38] is considered. An axial symmetric conductor is placed at the center of multiple coils with a sinusoidal excitation current. The geometry as well as the dimensions are shown in Figure 3.4 and Table 3.3. The workpiece (central conductor) is heated by the eddy current induced in the conductor, where the volume power density is contributed by the Joule losses $\dot{q} = \sigma \mathbf{E}^2$. It is assumed that the workpiece is cooled by convection and radiation. The convection is characterized by the convective boundary condition with the convective coefficient $h = 10 W / m^2 K$ and ambient temperature $T_a = 20°C$. The radiation of the workpiece is the heat flux density imposed on the conductor surface which is given by

25

$$q_s^{rad} = \varepsilon_w c_\sigma \left(T^4 - T_a^4 \right) \qquad (52)$$

where c_σ is the Stefan-Boltzmann constant ($5.670 \times 10^{-8} W / m^2 K^4$) and ε_w is the emissivity. For the simulated case, the value 0.97 was chosen as the emissivity. Other material properties used in the simulation are listed in Table 3.4. Note that the thermal conductivity κ, the specific heat C_p and the electrical conductivity σ are temperature dependent, whose values as a function of temperature are shown in Figure 3.5. From the measured values, those material properties can be fitted by polynomial functions. In the simulation, first-degree polynomials are used for the thermal conductivity and the specific heat, whereas a third-degree polynomial is used for the electric conductivity. To validate the EM-thermal coupling method, the simulation results are compared with the measurements as well as the results from COMSOL, as shown in Figure 3.6. In the test, the excitation current was set to 532 A rms at 26.8kHz. The steady-state temperature of the workpiece is 1212℃ (measured) and 1202℃ (simulated), which shows a good agreement.
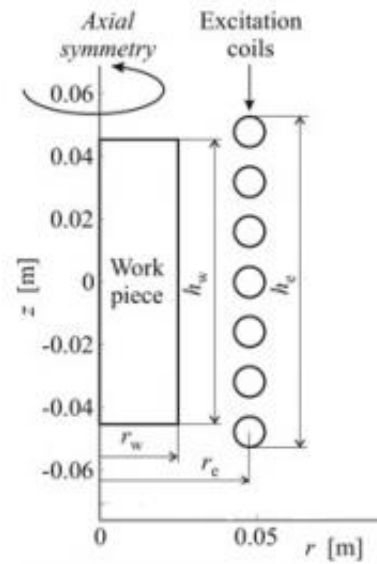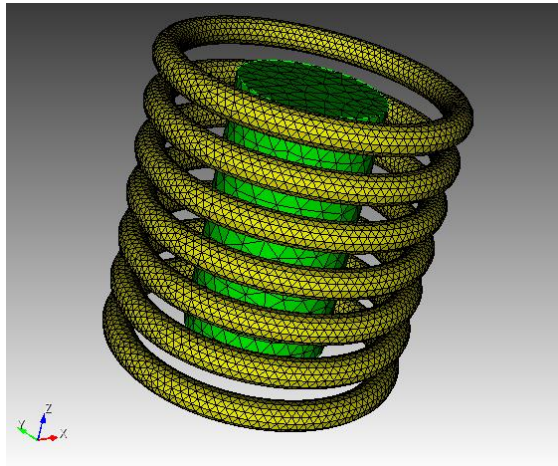

Figure 3.4 Geometry and dimensions of induction heating problem 1.

26

Table 3.3 Dimensions of the components in induction heating problem 1

Coil outer radius	r_e	47.4 mm
Conductor radius	r_w	25.0 mm
Conductor length	h_w	90.0 mm
Coil height	h_e	104.8 mm
Coil inner radius	a	4.8 mm

Table 3.4 Material properties for induction heating problem 1

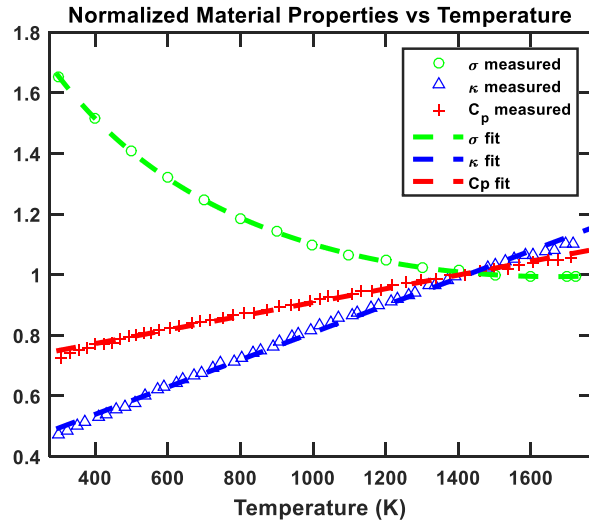| Mass density	ρ	$7350\ kg/m^3$
Thermal conductivity (1170°C)	κ	$30.3\ W/mK$
Heat capacity (1170°C)	C	$667\ J/kgK$
Electrical conductivity (1170°C)	σ	$0.799\ MS/m$

Figure 3.5 Electric conductivity, thermal conductivity and specific heat as a function of temperature; all material properties are normalized with respect to their values at 1170 ℃.
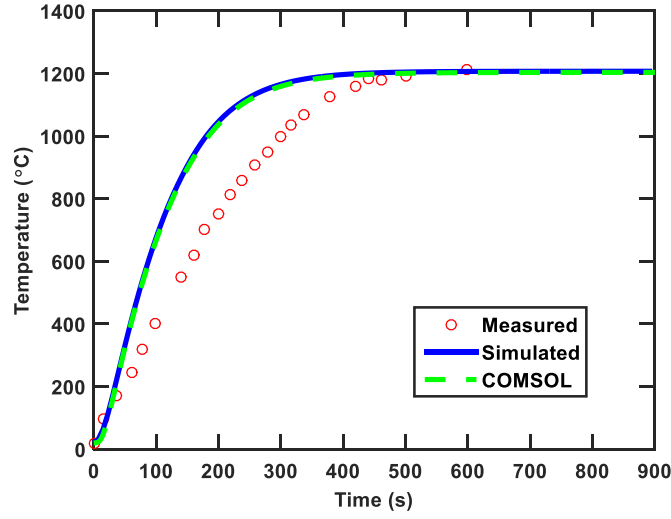
27

Figure 3.6 Workpiece temperature change in induction heating problem 1.

3.4.3   Induction Heating Problem 2

In this section, a benchmark problem [39] of nonlinear induction heating is considered. The geometry is given in Figure 3.7, and all the numerical data is listed. Different from the induction heating problem 1, the billet at the center of coils is made of C45 steel, which is a nonlinear material. The permeability of this material is not only a function of the magnitude of the magnetic field, which can be described by a B-H curve, but also strongly dependent on the temperature. In this work, the Frohlich model [40-42] is adopted, and it relates the magnetic flux density with the magnetic field by

$$\left|\mathbf{B}\right| = \left(\mu_0 + \frac{\alpha}{\beta + \left|\mathbf{H}\right|} \right)\left|\mathbf{H}\right| \tag{53}$$

where α and β can be expressed as a function of temperature:

$$\begin{aligned}
\alpha &= \begin{cases} \alpha_0 f(T) & \text{if } T < T_c \\ 0 & \text{if } T \geq T_c \end{cases} \\
\beta &= \begin{cases} \beta_0 / f(T) & \text{if } T < T_c \\ 0 & \text{if } T \geq T_c \end{cases}
\end{aligned} \tag{54}$$

28

In equation (54), $T_c = 770°C$ is the Curie temperature, after which the material will be demagnetized, and the relative permeability sharply drops to one. The function $f(T)$ in (54) is calculated with

$$f(T) = 1 - e^{(T-T_c)/C} \tag{55}$$

The constant C is selected for fitting the approximated curve with experimental data. The relative permeability as a function of temperature and magnetic field strength is fitted from the experiment data and plotted out in Figures 3.8 and 3.9.

Other parameters used in the EM-thermal simulation are also temperature dependent. The electrical resistivity and the thermal conductivity can be approximately considered as linear functions [43]:

$$\kappa(T) = \kappa_0 (1 + aT) \tag{56}$$

$$\sigma(T) = \frac{1}{\sigma_0 (1 + aT)} \tag{57}$$

The nonlinear relation between the heat capacity and temperature is more involved and the value is sharply uplift at the Curie point. It is approximated by an exponential function plus a Gaussian function as

$$C_p(T) = C_{pi} + (C_{p0} - C_{pi}) e^{-T/\tau} + E \cdot Gauss(T) \tag{58}$$

with

$$Gauss(T) = \frac{1}{a\sqrt{2\pi}} e^{-\frac{1}{2}\left(\frac{T-T_c}{a}\right)^2} \tag{59}$$

For the heat transfer process, the boundary condition of the temperature field includes the heat loss caused by convection and radiation, which were explained in the previous sections. For a convenient implementation of the boundary conditions, the effect of the radiation in equation (52) can be lumped into the convective boundary condition, which results in an equivalent convection coefficient:

29

$$h_{eq} = h + \varepsilon_w c_\sigma \frac{T^4 - T_a^4}{(T - T_a)} \qquad (60)$$

where the first term h comes from the convective boundary condition, and the second term corresponds to the radiation.

Figure 3.10 gives the coefficients as a function of temperature, where both experimental data and fitted curves are plotted. To excite the coil, a sinusoidal current at 2kHz is applied with amplitude of 3,500 ARMS, and the number of turns in the coil is 20. Two observation points are selected on the bottom surface of the billet, one at the center ($x = $ 0mm) and the other point on the boundary ($x = $ 30mm). Very good agreement is observed, as shown in Figure 3.11.

Coils

Billet axial length: 1000mm
Coil axial length: 1000mm
Billet radius: 30mm
Coil internal radius: 48mm
Coil turn axial length: 40mm
Coil turn radial width: 20mm

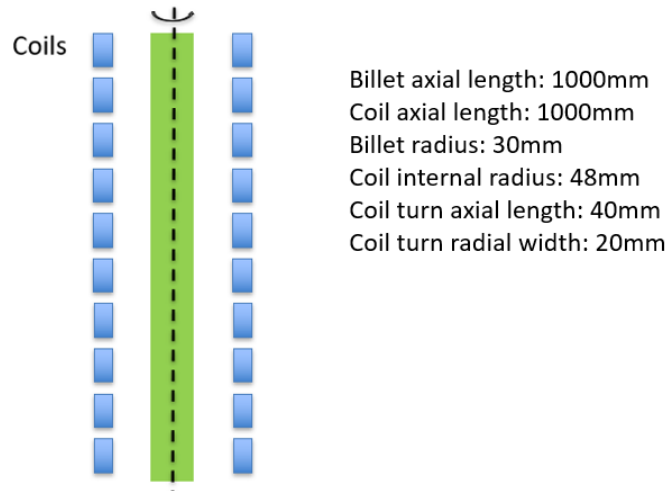*Figure 3.7 Geometry and dimensions of induction heating problem 2.*

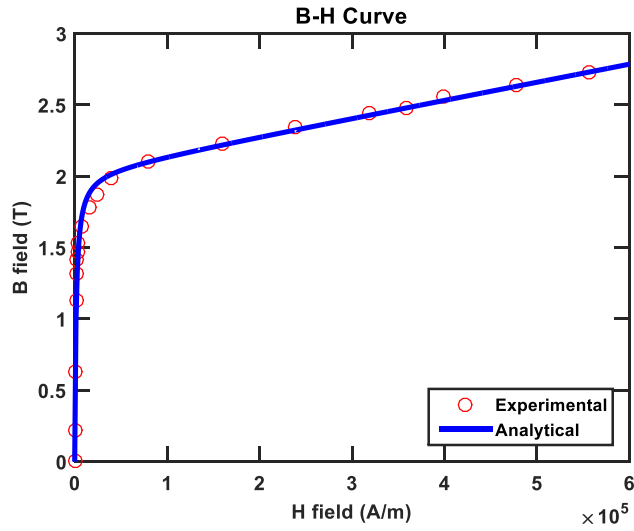*Figure 3.8 B-H curve at room temperature T = 20°C.*
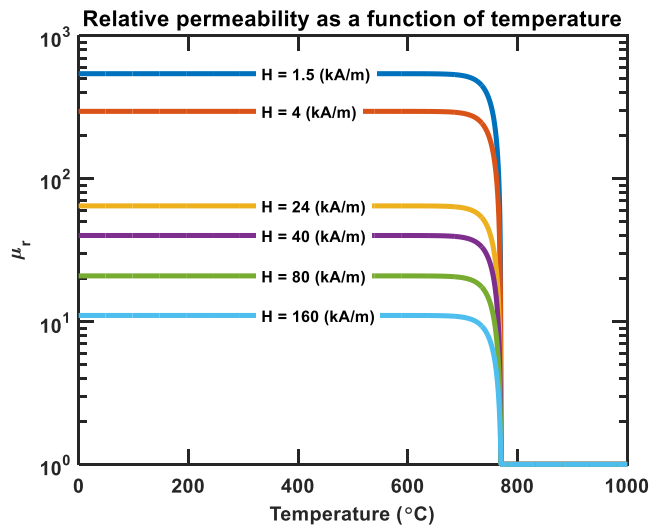

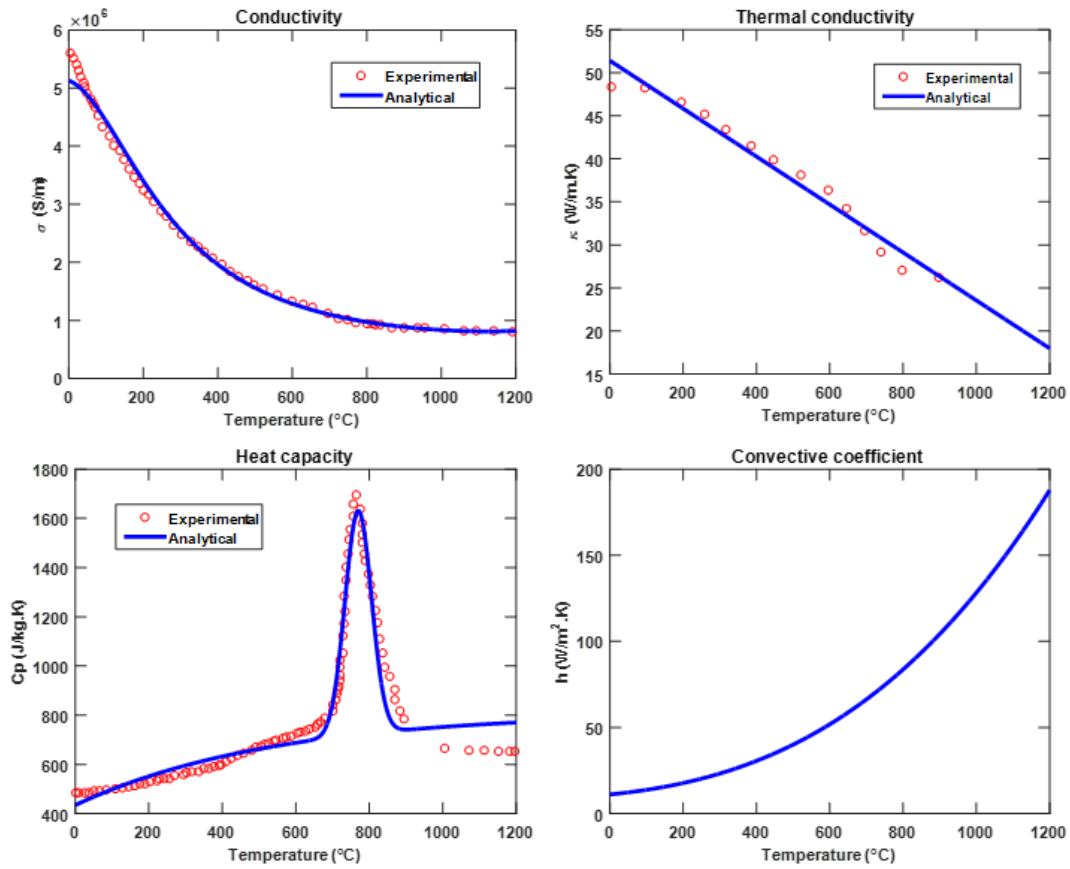*Figure 3.9 Relative permeability as a function of temperature under different magnetic field strength.*

Figure 3.10 Material properties of steel C45: Top left: electrical conductivity; Top right: thermal conductivity; Bottom left: specific heat capacity; Bottom right: equivalent convection coefficient.
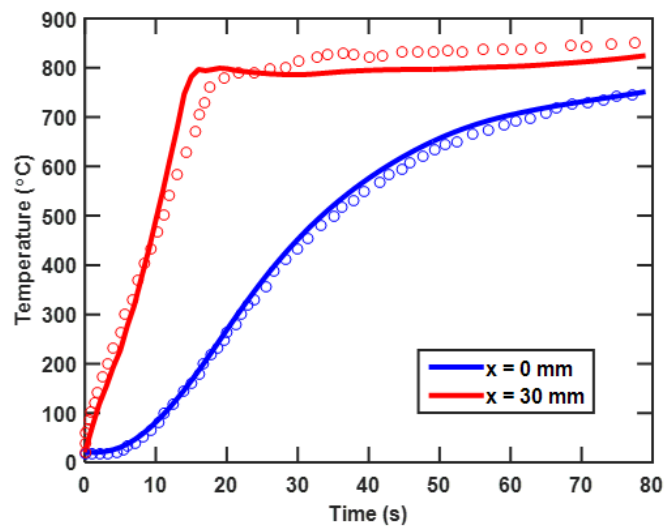

Figure 3.11 Transient temperature distribution at two observation points.

CHAPTER 4

CONCLUSION AND FUTURE WORK

In this thesis, nonlinear electromagnetic problems and EM-thermal simulation method have been investigated for the analysis of electric machines. The time-domain finite element method is employed for its capability of modeling complex geometries. In Chapter 2, a numerical solution to nonlinear problems is formulated. The second-order wave equation is solved with the magnetic vector potential as the unknown quantity, from which the electric and magnetic fields can be recovered. The resulting nonlinear equation is solved using the Newton-Raphson method. For nonlinear magnetic materials whose permeability can be described the B-H curves, polynomial functions are used to interpolate the B-H curve, and the Jacobian matrix can be readily found. However, when materials exhibit hysteresis phenomena, the formulation can be more involved. To include the hysteresis effect into the nonlinear solver, the J-A model is adopted, which relates total magnetization in the material with the magnetic field though an ordinary differential equation. At each time step, the Newton solver is invoked for the solution evolution. Within each Newton iteration, the ODE in the J-A model is first evaluated to update the permeability which is then plugged into the Jacobian matrix. Several numerical examples are presented to demonstrate the capability of the proposed formulation.

In Chapter 3, the electromagnetic-thermal co-simulation is discussed. EM losses lead to temperature increase in the system, and the temperature change, in turn, modifies the material properties, which results in a fully coupled EM-thermal problem. An efficient approach to couple the EM problem and heat transfer process is proposed. In the EM part, the Newmark-β method is adopted due to its unconditional stability. The time step is restricted by the frequency and chosen to be fine enough to capture the time variation of the electric and magnetic fields, which is on the order of milliseconds. The thermal part, however, has a much larger time-step size with an order of seconds to minutes. Different timescales are therefore applied to different processes. After each thermal time step, the material properties are first updated based on the temperature distribution and the EM problem is solved for several periods. When marching into the next thermal time step, the heat source is extrapolated from the EM losses to obtain the updated values, and the thermal system is solved again until a steady state is reached.

For the future work, further studies will be conducted to apply the proposed nonlinear EM-thermal coupling method to practical applications in motor designs. In this thesis, a preliminary investigation was done with solvers built up. Simple induction heating problems were used to verify the accuracy. However, when the approaches are to be applied to motor designs, more challenges will be encountered. The first problem one has to solve is how to deal with a significantly increasing number of unknowns as very small air gaps and sharp teeth are commonly seen in a motor, which results in extremely fine meshes and thus large number of unknowns. Second, the current method treated the entire domain as a nonlinear system, and the Newton-Raphson iteration will be very time consuming due to repeatedly updates of the Jacobian matrix. But in reality, only a small portion of the structure is made of nonlinear materials. Therefore, an efficient algorithm must be designed to split nonlinear and linear regions so that nonlinear solver is required only in the nonlinear region. One possible solution for these two problems is the domain decomposition method in which the entire domain is divided into small subdomains and each subdomain can be solved in parallel.

REFERENCES

[1] V. T. Buyukdegirmenci, A. M. Bazzi, P. T. Krein, "Evaluation of induction and permanent-magnet synchronous machines using drive-cycle energy and loss minimization in traction applications," *IEEE Trans. Ind. Appl.*, vol. 50, no. 1, 2014.

[2] K. Rajashekara, "History of electric vehicles in general motors," *IEEE Trans. Ind. Appl.*, vol. 30, no. 4, pp. 897-904, 1994.

[3] O. Dobzhanskyi, E. Mendrela, "PM AC motor with two degrees of mechanical freedom," *Tenth Annual Sigma Xi Student Research Conf.*, Raleigh, North Caroline, Nov. 13, 2010.

[4] O. Dobzhanskyi, E. Amiri and R. Gouws, "Comparison analysis of electric motors with two degrees of mechanical freedom: PM synchronous motor vs induction motor," *2016 II International Young Scientists Forum on Applied Physics and Engineering (YSF)*, Kharkiv, 2016, pp. 14-17.

[5] D. G. Dorrell, "Combined thermal and electromagnetic analysis of permanent-magnet and induction machines to aid calculation," *IEEE Tran. Ind. Electron.*, vol. 55, no. 10, pp. 3566-3574, Oct. 2008.

[6] L. Xu, H. Wang and P. T. Krein, "A high-performance permanent-magnet-free machine for wide load ranges," *2017 IEEE International Electric Machines and Drives Conference (IEMDC)*, Miami, FL, 2017, pp. 1-7.

[7] H. Cai, L. Gao and L. Xu, "Calculation of maximum torque operating conditions for inverter-fed induction machine using finite element analysis," *IEEE Tran. Ind. Electron.*, vol. 66, no. 4, pp. 2649-2658, April 2019.

[8] H.-T. Lee, L.-C. Fu, and H.-S. Huang, "Sensorless speed tracking of induction motor with unknown torque based on maximum power transfer," *IEEE Trans. Ind. Electron.*, vol. 49, no. 4, pp. 911–924, Aug. 2002.

[9] S. A. Odhano, R. Bojoi, A. Boglietti, Ş. G. Roşu, and G. Griva, "Maximum efficiency per torque direct flux vector control of induction motor drives," *IEEE Trans. Ind. Appl.*, vol. 51, no. 6, pp. 4415–4424, Nov. 2015.

[10] Y. W. Li, M. Pande, N. R. Zargari, and B. Wu, "An input power factor control strategy for high-power current-source induction motor drive with active front-end," *IEEE Trans. Power Electron.*, vol. 25, no. 2, pp. 352– 359, Feb. 2010.

[11] J. M. Jin, *The Finite Element Method in Electromagnetics*, Third Edition. Hoboken, NJ: Wiley, 2014.

[12] Y. Guan, Z. Q. Zhu, I. A. A. Afinowi, J. C. Mipo, and P. Farah, "Calculation of torque-speed characteristic of induction machine for electrical vehicle application using analytical method," *Proc. Int. Conf. Elect. Mach.*, pp. 2715–2721, Sep. 2014.

[13] A. Boglietti, A. Cavagnino, and M. Lazzari, "Computational algorithms for induction-motor equivalent circuit parameter determination—Part I: Resistances and leakage reactances," *IEEE Trans. Ind. Electron.*, vol. 58, no. 9, pp. 3723–3733, Sep. 2011.

[14] A. Boglietti, A. Cavagnino, and M. Lazzari, "Computational algorithms for induction motor equivalent circuit parameter determination—Part II: Skin effect and magnetizing characteristics," *IEEE Trans. Ind. Electron.*, vol. 58, no. 9, pp. 3734–3740, Sep. 2011.

[15] R. F. Harrington, *Field Computation by Moment Methods*. New York: Macmillan, 1968.

[16] E. K. Miller, L. Medgyesi-Mitschang, and E. H. Newman, Eds. *Computational Electromagnetics: Frequency-Domain Method of Moments*. New York: IEEE Press, 1992.

[17] K. S. Kunz and R. J. Luebbers, *The Finite Difference Time Domain Method for Electromagnetics.* Boca Raton, FL: CRC Press, 1994.

[18] A. Taflove and S. C. Hagness, *Computational Electrodynamics: The Finite Difference Time Domain Method (3rd edition)*. Norwood, MA: Artech House, 2005.

[19] N. M. Newmark, "A method of computation for structural dynamics," *J. Eng. Mech. Div., Proc. Am. Soc. Civil Eng.*, vol. 85, no. EM 3, pp. 67-94, July 1959.

[20] D. C. Jiles and D. L. Atherton, "Theory of the magnetisation process in ferromagnetics and its application to the magnetomechanical effect," *J. Phys. D: Appl. Phys.*, vol. 17, no. 6, pp. 1265-1281, June 1984.

[21] D. C. Jiles and D. L. Atherton, "Theory of ferromagnetic hysteresis," *Magnetism and Magnetic Materials*, vol. 61, pp. 48-60, Sep. 1986.

[22] I. D. Mayergoyz, "Dynamic Preisach models of hysteresis," *IEEE Trans. Magn.*, vol. 24, no. 6, pp. 2925-2927, Nov. 1988.

[23] G. Bertotti, "Dynamic generalization of the scalar Preisach model of hysteresis," *IEEE Trans. Magn.*, vol. 28, no. 5, pp. 2599-2601, Sep. 1992.

[24] D. G. Dorrell, "Combined thermal and electromagnetic analysis of permanent-magnet and induction machines to aid calculation," *IEEE Trans. Ind. Electron.*, vol. 55, no. 10, pp. 3566-3574, Oct. 2008.

[25] P. K. Vong and D. Rodger, "Coupled electromagnetic-thermal modeling of electrical machines," *IEEE Trans. Magn.*, vol. 39, no. 3, pp. 1614-1617, May 2003.

[26] W. Jiang and T. M. Jahns, "Coupled electromagnetic-thermal analysis of electric machines including transient operation based on finite element techniques," *IEEE Trans. Ind. Appl.*, vol. 51, no. 2, pp. 1880-1889, Mar. 2015.

[27] W. Jiang and T. M. Jahns, "Development of efficient electromagnetic-thermal coupled model of electric machines based on finite element analysis," in *Proc. IEEE IEMDC*, Chicago, IL, USA, May 2013, pp. 816–823.

[28] S. A. Semidey, Y. Duan, J. R. Mayor, R. G. Harley and T. G. Habetler, "Optimal electromagnetic-thermo-mechanical integrated design candidate search and selection for surface-mount permanent-magnet machines considering load profiles," *IEEE Trans. Ind. Appl.*, vol. 47, no. 6, pp. 2460-2468, Dec. 2011.

[29] D. G. Dorrell, D. A. Staton, J. Kahout, D. Hawkins, and M. I. McGilp, "Linked electromagnetic and thermal modelling of a permanent magnet motor," in *Proc. IEEE Power Electron. Mach. Drives Conf.*, Dublin, Ireland, Apr. 2006, pp. 536–540.

[30] D. G. Dorrell, D. A. Staton, and M. I. McGilp, "A combined electromagnetic and thermal approach to the design of electrical machines," in *Proc. Int. Conf. Elect. Mach. Syst.*, Nagasaki, Japan, Nov. 20–23, 2006.

[31] M. Kuczmann, "Using the Newton-Raphson method in the polarization technique to solve nonlinear static magnetic field problems," *IEEE Trans. Magn.*, vol. 46, no. 3, pp. 875-879, 2010.

[32] "Testing electromagnetic analysis methods (T.E.A.M.)," http://www.compumag.org/jsite/team.html, International Compumag Society.

[33] M. Mirzaei, M. Mirsalim and S. E. Abdollahi, "Analytical modeling of axial air gap solid rotor induction machines using a quasi-three-dimensional method," *IEEE Trans. Magn.*, vol. 43, no. 7, pp. 3237-3242, Jul. 2007.

[34] M. Amrhein and P. T. Krein, "Force calculation in 3-D magnetic equivalent circuit networks with a Maxwell stress tensor," *IEEE Trans. Energy Convers.*, vol. 24, no. 3, pp. 587-593, Sept. 2009.

[35] S. J. Salon, *Finite Element Analysis of Electrical Machines*. Norwell, MA: Kluwer, 1995.

[36] T. Zedler, A. Nikanorov and B. Nacke, "Investigation of relative magnetic permeability as input data for numerical simulation of induction surface hardening," *Int. Scientific Coloquium MEP 2008*, Hanover, 2008.

[37] S. N. Vladimirov, S. N. Zeman and V. V. Ruban, "Analytical approximations of thermal dependence of permeability of construction steels," *Proc. of Tomsk Univ.*, vol. 31, 2009.

[38] P. Sergeant, D. Hectors, L. Dupre and K. V. Reusel, "Thermal analysis of magnetic shields for induction heating," *IET Electric Power Appl.*, vol. 3, no. 6, pp. 543-550, Nov. 2009.

[39] P. Di Barba, M. E. Mognaschi, D. A. Lowther, F. Dughiero, M. Forzan, S. Lupi and E. Sieni, "A benchmark problem of induction heating analysis," *Int. J. Appl. Electrom.*, vol. 53, no. S1, pp. S139-S149, Feb. 2017.

[40] A. Bossavit and J. Verite, "The 'TRIFOU' Code: Solving the 3-D eddy-currents problem by using H as state variable," *IEEE Trans. Magn.*, vol. 19, no. 6, pp. 2465-2470, Nov. 1983.

[41] D. Labridis and P. Dokopoulos, "Calculation of eddy current losses in nonlinear ferromagnetic materials," *IEEE Trans. Magn.*, vol. 25, no. 3, pp. 2665-2669, May 1989.

[42] F. Bay, V. Labbe, Y. Favennec and J. L. Chenot, "A numerical model for induction heating processes coupling electromagnetism and thermomechanics," *Int. J. Numer. Meth. Engng.*, vol. 58, no. 6, pp. 839-867, Oct. 2003.

[43] Y. Favennec, V. Labbe, Y. Tillier and F. Bay, "Identification of magnetic parameters by inverse analysis coupled with finite-element modeling," *IEEE Trans. Magn.*, vol. 38, no. 6, pp. 3607-3619, Nov. 2002.

[44] Simscale Documentation. *https://www.simscale.com/docs/validation-cases/heat-transfer-electronic-design/*